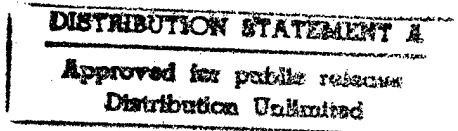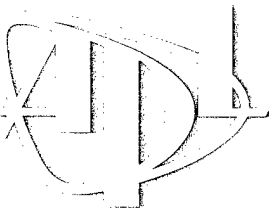# Bistatic Bottom Scattering: Model, Experiments, and Model/Data Comparison

by K.L. Williams and D.R. Jackson

Technical Report
APL-UW TR 9602
July 1997

Bistatic Bottom Scattering: Model, Experiments, and Model/Data Comparison

by K.L. Williams and D.R. Jackson

Applied Physics Laboratory   University of Washington
1013 NE 40th Street   Seattle, Washington 98105-6698

Acknowledgments

ABSTRACT

A model is presented for bistatic scattering from ocean sediments. It treats scattering due to both roughness of the seabed and volume inhomogeneities within the sediment. Accordingly, the scattered intensity is assumed to be a sum of two terms, one proportional to the roughness-scattering cross section and the other proportional to the volume-scattering cross section. The model is tested against data acquired as part of the Coastal Benthic Boundary Layer (CBBL) research program. As part of that program, an autonomous, circularly scanning sonar system was deployed in well-characterized regions. This sonar operated at 40 kHz, had a 5° horizontal beam, and acquired backscattering data over a 50-m radius. During part of the deployment, it operated in conjunction with a mobile receiving array so as to acquire bistatic data. The experimental apparatus and procedures are presented, and results are compared with model predictions.

TABLE OF CONTENTS

LIST OF FIGURES

Page

LIST OF TABLES

1. INTRODUCTION

The model for bistatic scattering from the seabed discussed in this report is an extension of the model for high-frequency backscattering strength presented by Jackson et al.[1] in 1986, improved by Mourad and Jackson,[2] and employed by Jackson and Briggs.[3] The model treated here is intended for use at high frequencies (10–100 kHz). A brief discussion of the bistatic model has been given by Jackson,[4] and references to prior work by other investigators can be found in Refs. 1–3.

Backscattering of high-frequency (10–100 kHz) acoustic energy from the seabed has been the subject of investigation for many years.[1] Recent interest in scattering geometries where the transmitter and receiver are not co-located has led to the development of a bistatic scattering model that incorporates much of the same physics as the backscattering model of Ref. 2. In particular, it includes contributions to scattering from both the rough sediment interface and inhomogeneities within the sediment. Both the model and its incorporation into an integral expression for bistatic scattered intensity are given in Section 2.

Tests of the bistatic model require both acoustic experiments in which specified geometries can be accurately realized and concurrent determination of the environmental parameters needed as inputs to the model. Such was the case in the experiments described in Section 3. Both backscattering (monostatic) and bistatic scattering experiments are described, since the bistatic model includes backscattering as a special case.

The fundamental quantity predicted by the model is the bistatic scattering strength. Section 4 compares model predictions and experimental results for two different sediments. The expression for the scattered intensity given in Section 2 plays a fundamental role in this comparison.

2. BISTATIC MODEL AND SCATTERED INTENSITY CALCULATIONS

The bistatic scattering strength model is presented in Section 2.1 and its incorporation into expressions for calculating scattered intensity in Section 2.2. The expressions for scattered intensity are the direct link between the model and the experiments, from which values for bistatic scattering strength are obtained using a method defined in Sections 2.2 and 4.

The bistatic scattering model is a generalization of a backscattering model that has been tested against data with good success.[1-3] The model treats scattering due to both roughness of the seabed and inhomogeneities in the sediment volume. Accordingly, the intensity is assumed to be a sum of two terms, one proportional to the roughness-scattering cross section and the other to the volume-scattering cross section. It is assumed that the acoustic penetration of the seabed is slight, so sediment volume scattering can be described as a surface process and quantified by an effective interface-scattering cross section.

A major assumption in the model is that the sediment can be treated as a lossy fluid; any effects due to elasticity or porosity are neglected. It is further assumed that there are no gradients in sediment properties, apart from the random fluctuations responsible for volume scattering. Thus the sediment can be characterized by three parameters: mass density, sound speed, and acoustic absorption coefficient. The seabed relief is assumed to be an isotropic, two-dimensional Gaussian random process completely determined by a spectral density that follows a simple power law in wavenumber. This adds two more parameters to the model: the exponent of the power law and a parameter that sets the overall spectral level. The volume scattering strength is also assumed to follow a power-law form, which adds the final three parameters to the model: the exponent of the power law, a parameter that sets the overall spectral level, and a parameter that relates density and compressibility fluctuations. Volume scattering is assumed to be weak in the sense that the scattered field is much smaller in magnitude than the incident field (defined as the field that would exist in the sediment in the absence of volume scattering).

The link between the bistatic scattering model and the experiments is the model for the intensity of scattering from the seabed as a function of time. The experiments used transmitters and receivers with known beam patterns and with measured separations, orientations, and heights above the bottom. The transmitted pulses were short (2 ms). In the experiments, the energy received at any point in time depends not only on the bistatic scattering cross section of the seabed but also on the geometrical parameters and the type of pulses used. The intensity model accounts for all these factors via an integration over the area of the seabed that is scattering energy into the receiver at any point in time. The results of this integration were directly compared with the experimental results, and, where appropriate (see Section 4), experimental values for bistatic scattering strength and the associated bistatic angles were extracted.

2.1. Bistatic Model

2.1.1. Definitions

The equation for bistatic scattering strength is of the form

$$S_b(\theta_s, \phi_s, \theta_i) = 10\log\left[\sigma_{br}(\theta_s, \phi_s, \theta_i) + \sigma_{bv}(\theta_s, \phi_s, \theta_i)\right],\tag{1}$$

where log is base 10 and $\sigma_{br}(\theta_s, \phi_s, \theta_i)$ and $\sigma_{bv}(\theta_s, \phi_s, \theta_i)$ are, respectively, the rough-ness and volume contributions to the scattering cross section per unit area. The angles θ_s, ϕ_s, and θ_i are defined in Figure 1. The incident grazing angle is denoted θ_i, the scattered grazing angle is denoted θ_s, and the bistatic angle, defined as the difference in azimuth between the incident and scattered directions, is denoted ϕ_s. In general, one needs four angles to describe bistatic scattering, two grazing angles and two azimuths; however, only the azimuthal difference is needed here because bottom statistics are assumed to be trans-versely isotropic. Later expressions for the scattering cross section will employ the follow-ing geometric parameters:

$$\Delta_t = \frac{1}{2}\left[(\cos\theta_i)^2 - 2\cos\theta_i\cos\theta_s\cos\phi_s + (\cos\theta_s)^2\right]^{1/2}\tag{2}$$

and

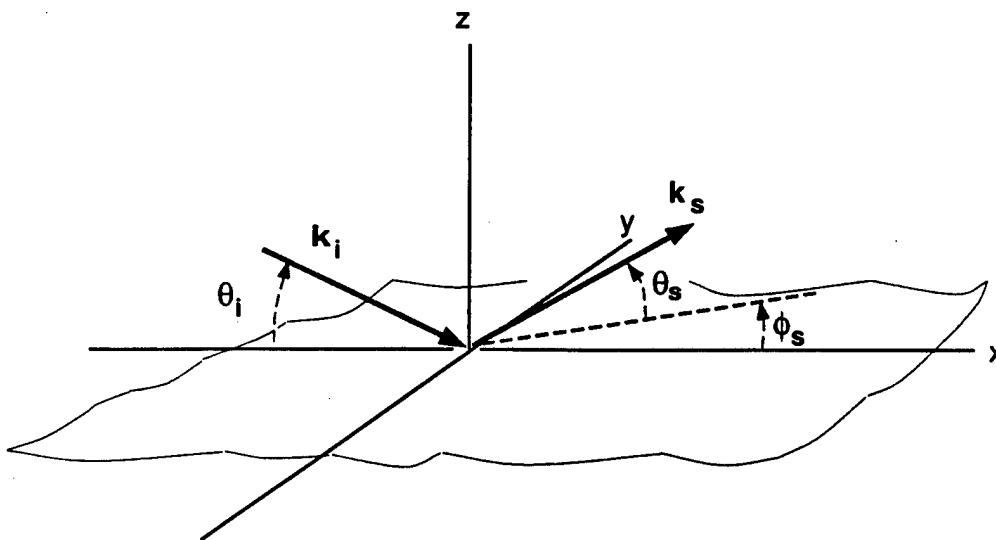$$\Delta_z = \frac{1}{2}(\sin\theta_i + \sin\theta_s).\tag{3}$$

Figure 1. Definition of bistatic angles.

These dimensionless parameters are proportional, respectively, to the transverse and vertical components of the change in the acoustic wave vector upon scattering. A parameter proportional to the magnitude of the change is also used.

$$\Delta = \sqrt{\Delta_t^2 + \Delta_z^2}.\tag{4}$$

The bistatic model treats the sediment as a fluid which is homogeneous except for the fluctuations responsible for volume scattering. The mean values of fluid properties are defined by three dimensionless ratios, ρ, ν, and δ. These are, respectively, the sediment/water density ratio, the sediment/water sound-speed ratio, and the ratio of imaginary to real wavenumber in the sediment. The statistics of the sediment properties are assumed to be spatially stationary. Thus the ratios defined above are independent of position; that is, there are no gradients in the mean parameters.

The surface roughness part of the bistatic model uses the Kirchhoff approximation near the specular direction. In other directions, it employs the small-roughness perturbation approximation. Bottom roughness is assumed to be a spatially stationary random process described by a two-parameter, isotropic, two-dimensional roughness spectral density:

$$W(K) = \frac{w_2}{(h_0 K)^{\gamma_2}},\tag{5}$$

where K is the magnitude of the two-dimensional wave vector and the spectrum is normalized so that the integration over a finite region in K-space gives the mean-square vertical deviation of the seabed from the mean plane due to those Fourier components included in the integration. The exponent is restricted to the range

$$2 \le \gamma_2 \le 4.\tag{6}$$

The parameter w_2 in Eq. 5 gives the strength of the spectrum and has dimensions (length).[4] The parameter h_0 is simply a reference length needed to balance dimensions in the equation. It is assigned the numerical value 1 and hence does not appear in calculations.

The volume-scattering portion of the bistatic model is an improvement on the backscattering phenomenological approach.[1-3] The bistatic model uses perturbation theory for volume scattering along the lines developed by Ivakin and Lysanov,[5] Hines,[6] Tang,[7] and Lyons et al.[8] Where the older backscatter model employed a single parameter to quantify sediment volume scattering strength, the bistatic model requires three parameters to characterize spectra for inhomogeneities in density and compressibility. The spectrum for density fluctuations is taken to be of the same power-law form as the roughness spectrum:

$$W_{\rho\rho}(k) = \frac{w_3}{(h_0 k)^{\gamma_3}}. \tag{7}$$

This spectrum is isotropic and normalized such that an integral over a finite volume of k-space yields the mean-square density fluctuation divided by the square of the mean density. Compressibility fluctuations are treated analogously and are assumed to be proportional to the density fluctuations. This is equivalent to the assumption used by other authors.[5,8] Thus the spectrum of compressibility fluctuations is

$$W_{KK} = \mu^2 W_{\rho\rho}, \tag{8}$$

and the cross spectrum is

$$W_{\rho K} = \mu W_{\rho\rho}, \tag{9}$$

where μ is a dimensionless parameter and is one of the eight environmental parameters needed to calculate bistatic scattering when using the present model. These eight parameters are defined in Table 1 and were described in the third paragraph of Section 2. Also given in Table 1 are the numerical values used for these parameters (see Section 3.4) for the two sites examined experimentally. With these definitions in hand, we are now ready to discuss the roughness and volume cross sections of Eq. 1.

Table 1. Bottom parameters used as model inputs.

Symbol	Definition	Short Name	Eckernförde	Panama City
ρ	Ratio of sediment mass density to water mass density	Density Ratio	1.18	1.97
ν	Ratio of sediment sound speed to water sound speed	Sound Speed Ratio	0.991	1.126
δ	Ratio of imaginary wavenumber to real wavenumber for the sediment	Loss Parameter	0.00186	0.0166
γ_3	Exponent of sediment inhomogeneity spectrum	Inhomogeneity Exponent	4	4
w_3	Strength of sediment inhomogeneity spectrum (cm^3) at wavenumber $(2\pi)/\lambda = 1$ cm^{-1}	Inhomogeneity Strength	0.00013	0.0000161
μ	Ratio of compressibility to density fluctuations in the sediment	Fluctuation Ratio	−0.69	−2.44
γ_2	Exponent of the bottom relief spectrum	Spectral Exponent	3.420	3.12
w_2	Strength of bottom relief spectrum (cm^4) at wavenumber $(2\pi)/\lambda = 1$ cm^{-1}	Spectral Strength	0.00231	0.00849

2.1.2. *Bistatic Roughness Scattering*

In this section, expressions are presented for the bistatic cross sections in the Kirchhoff and perturbation approximations. The net cross section, $\sigma_{br}(\theta_s, \phi_s, \theta_i)$, appearing in Eq. 1 is formed by smooth interpolation between the Kirchhoff cross section near the specular direction and the perturbation-theory cross section elsewhere. The interpolation between these two approximations is defined so that the smaller cross section takes precedence. This procedure is based on the fact that, for power-law spectra, the perturbation approximation overpredicts scattering near the specular direction owing to the singularity in the relief spectrum at zero wavenumber. In contrast, the Kirchhoff approximation tends to overpredict in other directions.[9] The interpolation scheme used here is

$$\sigma_{br}(\theta_s, \phi_s, \theta_i) = [\sigma^\eta_{kr}(\theta_s, \phi_s, \theta_i) + \sigma^\eta_{pr}(\theta_s, \phi_s, \theta_i)]^{1/\eta}, \qquad (10)$$

with $\eta = -2$. The σ_{kr} and σ_{pr} cross-section expressions are defined next and are standard results, expressed here in notation convenient to the bistatic application.

2.1.2.1 Kirchhoff Approximation

Analogous to the monostatic expression used by Jackson et al.,[1] the bistatic Kirchhoff cross section[10,11] can be expressed in the following form:

$$\sigma_{kr}(\theta_s, \phi_s, \theta_i) = \frac{|R(\theta_{is})|^2}{8\pi} \left(\frac{\Delta^2}{\Delta_z \Delta_t}\right)^2 \int_0^\infty e^{-qu^{2\alpha}} J_0(u) \, u \, du, \qquad (11)$$

where

$$q = 2k^2 \Delta_z^2 C_h^2 (2k\Delta_t)^{-2\alpha}. \qquad (12)$$

In Eq. 11, $J_0(u)$ is the zeroth-order Bessel function of the first kind and k is the acoustic wavenumber in water. The parameters α and C_h are roughness structure function parameters related to γ_2 and w_2 as follows:

$$\alpha = \frac{\gamma_2}{2} - 1 \qquad (13)$$

and

$$C_h^2 = \frac{2\pi w_2 \Gamma(2-\alpha) 2^{-2\alpha}}{h_0^{\gamma_2} \alpha (1-\alpha) \Gamma(1+\alpha)}. \qquad (14)$$

The function $R(\theta_{is})$ is the complex plane-wave reflection coefficient (the so-called Rayleigh or Fresnel reflection coefficient) for a flat interface separating water and sediment. It can be expressed in terms of the parameters ρ, ν, and δ^2 and is evaluated at the grazing angle

$$\theta_{is} = \text{asin}(\Delta),$$

(15)

where Δ is defined in Eq. (4). This angle is not the actual incident or scattered grazing angle relative to the horizontal; rather, it is the grazing angle that would result if the seabed were tipped in such a way as to provide specular reflection between the transmitter and receiver. Thorsos (private communication) finds that this value gives improved accuracy compared to other choices, as reflection from suitably oriented facets tends to dominate the scattering process near the specular direction.

2.1.2.2 Perturbation Approximation

The bistatic backscattering cross section computed in the perturbation approximation[1-3,12,13] can be put in the following form[14]:

$$\sigma_{pr}(\theta_s, \phi_s, \theta_i) = \frac{1}{4}k^4 |1 + R(\theta_i)|^2 |1 + R(\theta_s)|^2 |G|^2 W(2k\Delta_t).$$

(16)

Equation 16 involves the reflection coefficient and roughness spectral density discussed earlier. The argument of the roughness spectral density is the "Bragg wavenumber." The complex function G is

$$G = \left(\frac{1}{\rho} - 1\right)\left[\cos\theta_i \cos\theta_s \cos\phi_s - \frac{P(\theta_i)P(\theta_s)}{\rho}\right] + 1 - \frac{\kappa^2}{\rho}.$$

(17)

In Eq. 17,

$$\kappa = \frac{1 + i\delta}{\nu}$$

(18)

is the complex wavenumber in the sediment divided by the real wavenumber in water and

$$P(\theta) = \sqrt{\kappa^2 - (\cos\theta)^2}.$$

(19)

2.1.3. Sediment Bistatic Volume Scattering

Mourad and Jackson[2] used a volume-scattering expression similar to that of Stock-hausen[15] in their backscatter model. The bistatic equivalent is readily obtained. It relates the sediment volume-scattering cross section, σ_v, to the effective interface bistatic-scattering cross section, $\sigma_{bv}(\theta_s, \phi_s, \theta_i)$, appearing in Eq. 1.

$$\sigma_{bv}(\theta_s, \phi_s, \theta_i) = \frac{\left|1 + R(\theta_i)\right|^2 \left|1 + R(\theta_s)\right|^2 \sigma_v}{2k\rho^2 Im\left[P(\theta_i) + P(\theta_s)\right]}. \tag{20}$$

Perturbation theory is used to obtain the volume-scattering cross section, σ_v. Adapting a result given by Ishimaru[16] to the present situation and using Eqs. 7–9 yields

$$\sigma_v = \frac{\pi}{2}k^4 \left|\mu\kappa^2 + \cos\theta_i \cos\theta_s \cos\phi_s - P(\theta_i)P(\theta_s)\right|^2 W_{\rho\rho}(\Delta k). \tag{21}$$

Acoustic loss in the sediment has been included by allowing the wavenumber in the sediment to be complex. The spectrum $W_{\rho\rho}$ is evaluated at the Bragg wavenumber for volume scattering, which is the magnitude of the difference between the real parts of the incident and scattered three-dimensional wave vectors (defined in the sediment).

$$\Delta k = k \left|4\Delta_t^2 + \left\{Re\left[P(\theta_i) + P(\theta_s)\right]\right\}^2\right|^{1/2}. \tag{22}$$

2.2. Scattered Intensity

The experiments described in Section 3 use a directional receiver and a directional source that emits a short FM slide. To determine values for the bistatic scattering strength from these experiments, an expression for the bistatic scattered intensity as a function of time was derived in terms of the bistatic cross sections given in Eq. 1. The expression given below is the scattered intensity $I(t)$ of a short-duration, or "impulse," pulse. This expression must be convolved with the signal transmitted (intensity vs time) to obtain predictions of the absolute levels and temporal structure of the scattered intensity for any experiment.

The impulse response is

$$I(t) = I_0 \iint \left[\frac{(\sigma b_x b_r)}{(D_1 D_2)^2} 10^{-\frac{\alpha_w(D_1 + D_2)}{10}}\right] dx\, dy \tag{23}$$

(see definitions in Figure 2). Here, σ is the sum of the surface- and volume-scattering cross sections appearing in Eq. 1, α_w is the attenuation of sound in water for the frequency of

interest in decibels per unit length, b_x and b_r are the beam patterns of the transmitter and receiver, respectively, and D_1 and D_2 are the distances shown in Figure 2. The source is assumed to emit a rectangular pulse of infinitesimal length dt that has intensity I_0 at a range of 1 m.

$$D_2{}^2 = (x - x_2)^2 + y^2 + d_2{}^2$$

$$dx = \left(\frac{dx}{dD} \bigg|_y \right) \Delta D$$
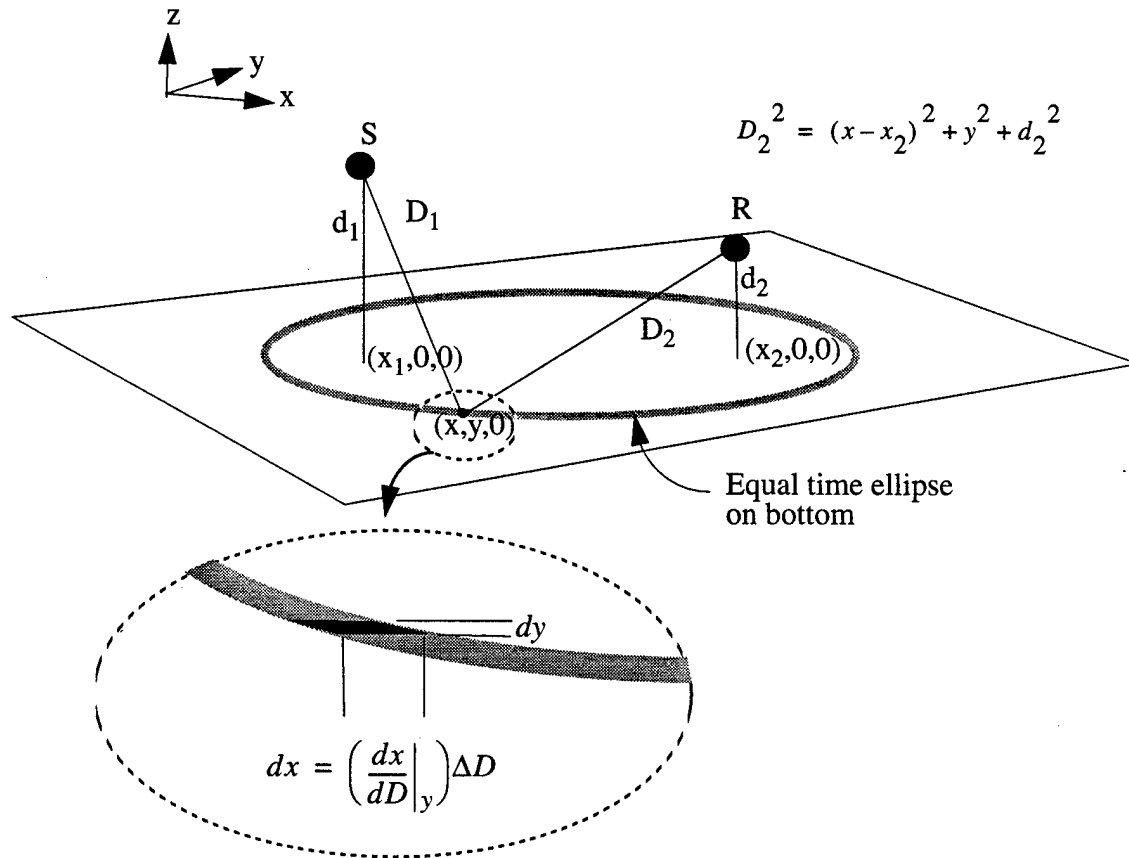
Figure 2. Bistatic geometry and definitions of variables

The integrations in Eq. 23 are over the infinitesimal area lying between the two ellipses, which have associated travel times t and $t + dt$ from transmitter to seabed to receiver. Therefore the limits on the x and y integrations in Figure 2 are actually functions of time. Furthermore, at any time t, the position x can be written as a function of y. Thus, as shown next, the integral in Eq. 23 can be rewritten as a pair of one-dimensional integrals over y.

Using the variable

$$D = D_1 + D_2 = ct, \tag{24}$$

where c is the speed of sound in water, the relation between x and y for a given t (or equivalently D) can be put in the form of an equation for an ellipse.

$$\frac{(x - x_o)^2}{a^2} + \frac{y^2}{b^2} = 1, \tag{25}$$

with

$$a = \frac{Q}{\varepsilon}, \tag{26a}$$

$$b = \frac{Q}{2D}, \tag{26b}$$

$$x_0 = -\frac{\beta}{2\varepsilon^2}, \tag{26c}$$

$$\varepsilon = 2\sqrt{D^2 - (x_1 - x_2)^2}, \tag{26d}$$

$$\beta = 4(x_2 - x_1)(x_2^2 - x_1^2 + d_2^2 - d_1^2 - D^2) - 8x_1 D^2, \tag{26e}$$

$$Q = D\sqrt{\frac{[D^2 - (x_1 - x_2)^2 - d_1^2 - d_2^2]^2 - 4d_1^2 d_2^2}{D^2 - (x_1 - x_2)^2}}. \tag{26f}$$

Using the enlargement of the $(x,y,0)$ region shown in Figure 2 and Eqs. 24 and 25 allows Eq. 23 to be rewritten as

$$I(t) = I_0(\Delta D) \int_{-b}^{b} \left[\frac{\left|\frac{dx}{dD}\right|(\sigma b_x b_r)}{(D_1 D_2)^2} 10^{-\frac{\alpha_w D}{10}} \right] dy, \tag{27}$$

where dx/dD can be calculated using Eq. 25. Equation 27 was numerically implemented using the measured beam patterns of the source and receiver and was used as described in Section 4 to obtain experimental values of the bistatic scattering strength. It is important to note that in practice two integrals are calculated using Eq. 27, since x is double valued in y; i.e., from Eq. 25,

$$x = x_o \pm a\sqrt{1 - \frac{y^2}{b^2}}. \tag{28}$$

3. BISTATIC EXPERIMENTS

Sections 3.1 and 3.2 describe the transmitter and receivers used in obtaining the backscattering and bistatic scattering results presented in Section 4. Section 3.3 describes a typical data-acquisition cycle. Section 3.4 describes the sites where the experiments were conducted; included in that section are numerical values for the parameters in Table 1.

3.1. The Benthic Acoustic Measurement System

The Benthic Acoustic Measurement System (BAMS) (Figure 3a) operates at 40 kHz and acquires data on acoustic backscattering from a circular region whose radius is set by surface reverberation. The system employs a planar transmitter/receiver array mounted on a rotator mechanism at the top of a 5-m-high tripod. All system operations are under control of an on-board computer with a data-storage capacity of approximately 120 Mbyte. Storage batteries provide sufficient energy to operate the computer, electronics, and rotator for the time required to reach the limit of the data-storage capacity. This time may be days or months, depending on the rate at which data are acquired. In the experiments reported here, the interval between sonar scans was variously set at 20 min, 30 min, and 1 hour, and each
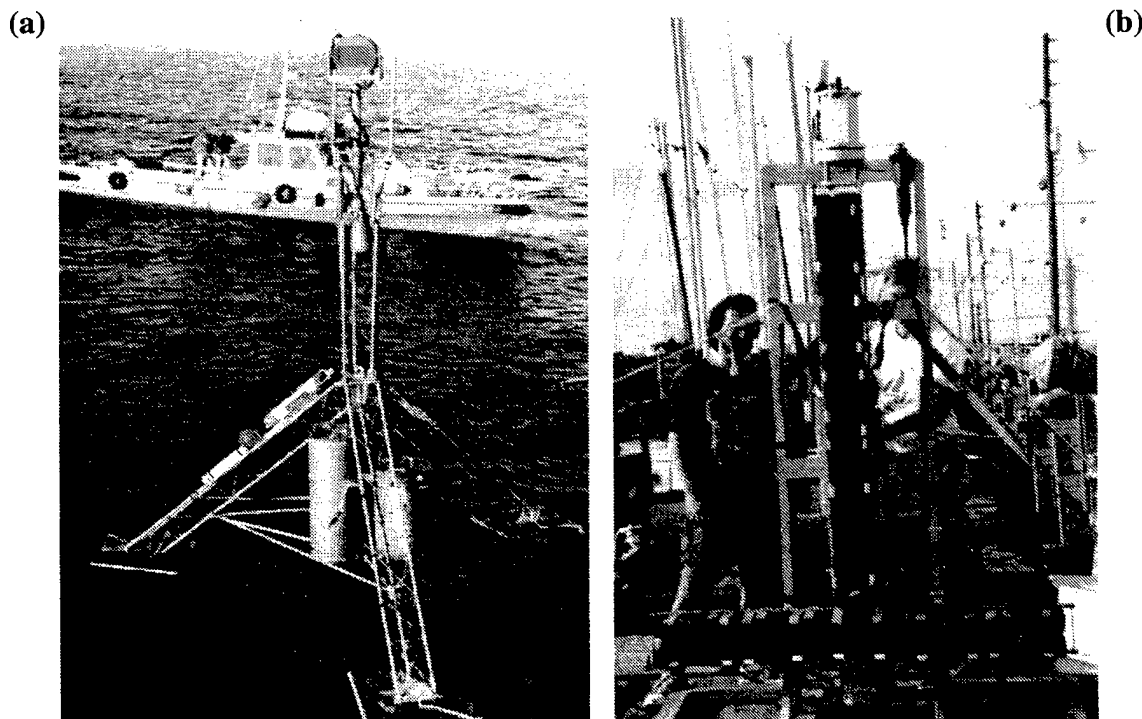
(a)   **(b)**

Figure 3. Benthic Acoustic Measurement System (a) and mobile receiving arrays (b).

scan covered a full 360° in 72 steps of 5°. The 5° step increment was chosen on the basis of the horizontal directivity patterns of the transmitter and receivers, which were essentially identical in the horizontal plane with a full width of 6.5° at one-half maximum power. The full array aperture was used for transmission, giving a vertical directivity pattern with a full width of 14° at one-half maximum power. For reception, the aperture was divided into upper and lower halves, yielding vertical directivity patterns of 27° for the receivers. The levels of the first vertical sidelobes were down 13–15 dB relative to the main lobe for the various directivity patterns. The maximum response axis of the array was depressed approximately 12.5° below the horizontal. Because the tower was not perfectly vertical, the depression angle varied slightly as the transducer was rotated. A pendulum potentiometer measured the depression angle at each step in each scan. The azimuthal orientation of the apparatus was measured by an on-board fluxgate compass and by a magnetic compass mounted on the array which was read visually by divers assisting in the deployment. The time interval between rotational steps was 5 s, of which about 2 s were required to achieve the change in direction. The remaining time allowed the transmitter/receiver array to come to complete rest before each transmission.

The transmitted signal was a 2-ms-long, FM waveform with a constant amplitude over its duration. During this 2-ms interval, the frequency was swept from 39 to 41 kHz. The transmitter provided a source level of 217 dB re 1 μPa/m. The transmitted waveform was digitized and stored for each transmission. These data show that the transmitter voltage remained constant to within a small fraction of 1 dB during each experiment. Each of the two receiver channels was digitized with an interval between samples equal to one quarter of a cycle at 40 kHz. Pairs of adjacent samples were saved every 0.5 ms to provide a pass-band complex signal.[17] This sampling rate is very close to the limit imposed by the sampling theorem for bandlimited signals, and some aliasing occurred as a result. Sampling was started 10 ms prior to signal transmission; these early samples were used to estimate the noise level. The sampling window extended to 81 ms after transmission, which allowed digitization of approximately 1400 circular scans before the data storage capacity of the system was exceeded. Digitization and signal generation are controlled by a single clock. This makes it possible to make sensitive comparisons between echoes acquired in separate scans, even when the scans are weeks apart. Such processing has been used to obtain remote temperature measurements[18] and to observe changes in the seabed.[19] The backscattering results to be presented in Section 4 are derived from this data set.

3.2. Mobile Bistatic Receiving Arrays

During the bistatic measurements, the ship-mounted mobile, steerable arrays shown in Figure 3(b) were also deployed. The array on the BAMS tripod served as the transmitter, and the ship-deployed arrays served as receivers. The receiving arrays were steered by means of a hydraulically controlled rotator, which can be seen at the top of the arrays in

Figure 3(b). The hydraulic controls were available during data acquisition, so different geometries could be obtained within a data-acquisition cycle (see next section).

The mobile arrays were divided in quadrants, each 32 cm long. The narrow and wide beamwidths of the quadrants were 8° and 37°. The bistatic data were acquired with the horizontal array, with each quadrant being recorded separately at two different gains to increase the dynamic range. The analog signals were conditioned using the APL MAME system[20]; the conditioned data were recorded using LabVIEW software controlling National Instruments data-acquisition boards.[21]

3.3. Data Acquisition Cycle

A simplified diagram of the bistatic experiment is shown in Figure 4. The three independent bistatic angles (θ_i, θ_s, ϕ_s) are also shown in the figure. The mobile array was suspended from the tending vessel, which was placed in a one-point moor near the BAMS tripod. It is necessary to use a mobile receiving array to obtain a statistically significant number of bistatic-scattering cross-section measurements in any region of bistatic scattering angle space. The horizontal distance between the source and receivers ranged from 20 to 100 m. In the data presented here, the horizontal distance was always less than 60 m.

A data cycle consisted of taking data with the mobile array during a 360° rotation of the tripod array. This rotation comprises 72 positions (5° increments) at each of which the 40-kHz signal was emitted. As shown in Figure 4, the mobile array was steered so that the centers of the transmit and receive beams intersected each other on the seabed.
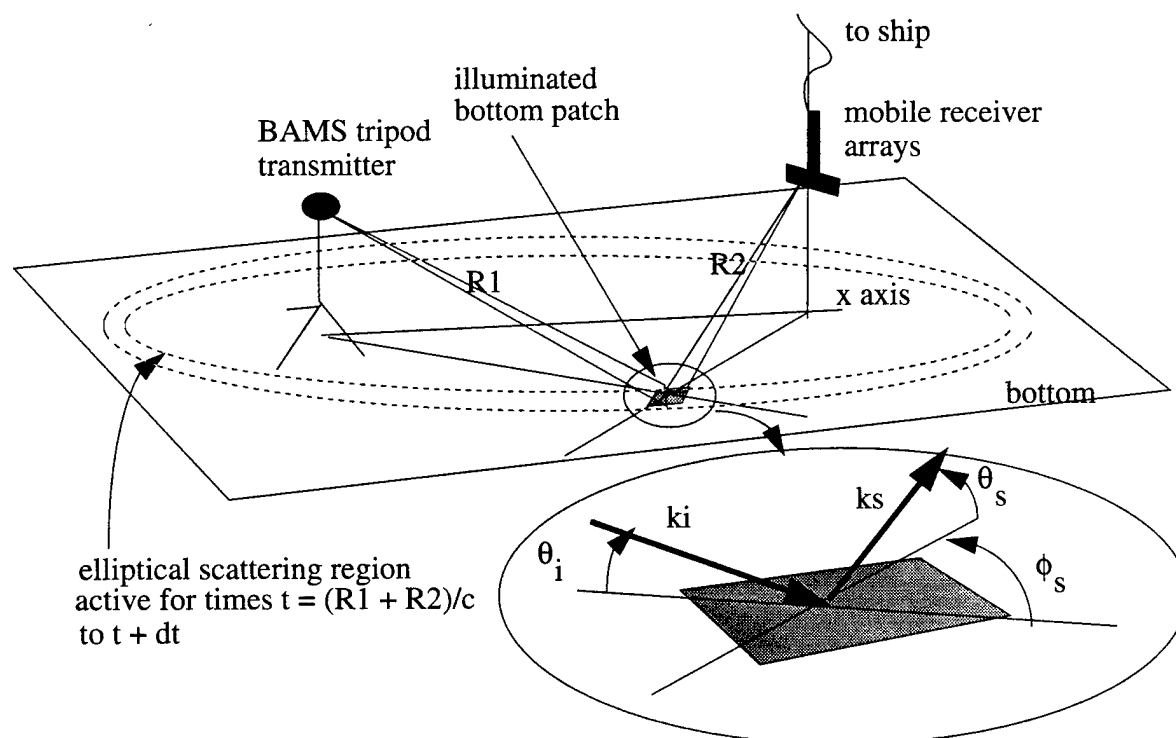

Figure 4. Diagram of bistatic scattering experiment.

One primary data-analysis effort was determining the bistatic angles from the data set. Measuring all the geometrical parameters needed to determine the bistatic angles obtained during each data run requires the use of the split-beam phase from the receiver-array quadrants (time resolved to ±5 µs) as well as several supplemental devices, including compasses (accurate to within ±2°), ranging transducers (±1 m), an altimeter (±30 cm), a pressure gauge (±30 cm), and inclinometers (±0.1°). The largest uncertainty in the experiment is in the ranging since it could not be performed on a ping-by-ping basis. The range was acquired an average of once every 5–10 pings. Because of this, data taken when the receiving array moved significantly (>3 m) between range measurements were not processed. The uncertainty in range is felt to be on the order of 2 m on the data set with the most receiver movement. The uncertainties quoted for the altimeter and pressure gauge come from side-by-side measurements at 10 depths throughout the water column in which the difference between the two results had a standard deviation of 26 cm. The uncertainty quoted for the compass is greater than that claimed by the manufacturer but is felt to be realistic given the calibration of the compass while embedded in the receiver apparatus shown in Figure 3. The inclinometers were also calibrated while on the receiver array by use of a digital inclinometer with ±0.01° accuracy.

The bistatic scattering strengths given in Section 4 were derived by comparing the pressures received at the face of the mobile arrays with those predicted by simulations of the experiment that used Eq. 27, the experimental geometry, the transmitted pulse length, and the beam patterns of the receiving and transmitting arrays.

3.4. Experimental Sites

3.4.1. Eckernförde Bay

The properties of the sediment at this site are documented in Ref. 22. The sediment had a very high water content, with a porosity of approximately 85%, and rather low acoustic attenuation (0.18 dB/kHz/m).[23] The most striking acoustic feature at this site was a layer of free methane bubbles with an upper boundary 0.5 to 2.0 m below the sediment/water interface.[24,25] The size distribution of these bubbles was measured using computer tomography,[26] and estimates from these data indicate that volume-scattering strengths should be very high, between –10 and –20 dB/m.[27] Tang et al.[28] have shown that these gas bubbles are the principal cause of backscattering at 40 kHz. This is due to the combination of low attenuation and high volume-scattering strength. The model parameters for this site (Table 1) were determined as part of the CBBL program and, with one exception (discussed below), are those given in Ref. 29. *In situ* acoustic probes were used to determine the values for the compressional-wave velocity and attenuation in the sediment. Diver cores were used to determine sediment density, and underwater photography was used to determine the surface-roughness parameters. From comparisons of the backscattering data with the backscatter model of Ref. 2, it was determined that surface-roughness effects played only a small role in backscattering from this sediment (a result consistent with Ref. 28). The vol-

ume scattering used in the present model (characterized by γ_3, w_3, and μ) comes from a perturbation analysis, and bubble scattering does not fit this assumption. However these volume parameters can be regarded as phenomenological rather than physical and can be used to obtain an initial estimate of the bistatic scattering. In this regard, the w_3 parameter quoted in Table 1 is not the one found in Ref. 29. It was adjusted to give good initial estimates of the intensity time series from which bistatic scattering strengths are derived (see Section 4.2).

3.4.2. Panama City

This was a coarse sand site. The parameters shown in Table 1 are those given in Ref. 29. The techniques used to determine the environmental parameters were similar to those used at the Eckernförde Bay site. Note that the model predictions are dominated by the measured parameters ρ, v, δ, γ_2, and w_2 for this site.

4. MODEL/DATA COMPARISONS

The objective of the model/data comparisons was to obtain experimental values for the bistatic scattering strength and compare them with the model predictions. For each transmission, the geometry information recorded at the time of transmission, the attenuation in the water, the beam patterns of the source and receiver, and the values for the bistatic cross section predicted using Table 1 were used in Eq. 27 to obtain an impulse response by numerical integration. This result was convolved with the transmitted waveform to predict the amplitude and temporal structure of the intensity scattered from the seabed into the receiver. This prediction was then compared with its experimental counterpart. Two typical examples from the Panama City sand site are shown in Figures 5a (near forward scattering) and 5c (near backscattering). Calculations of the time and amplitude of the direct arrival and the signal scattered from the air/water interface are also shown.
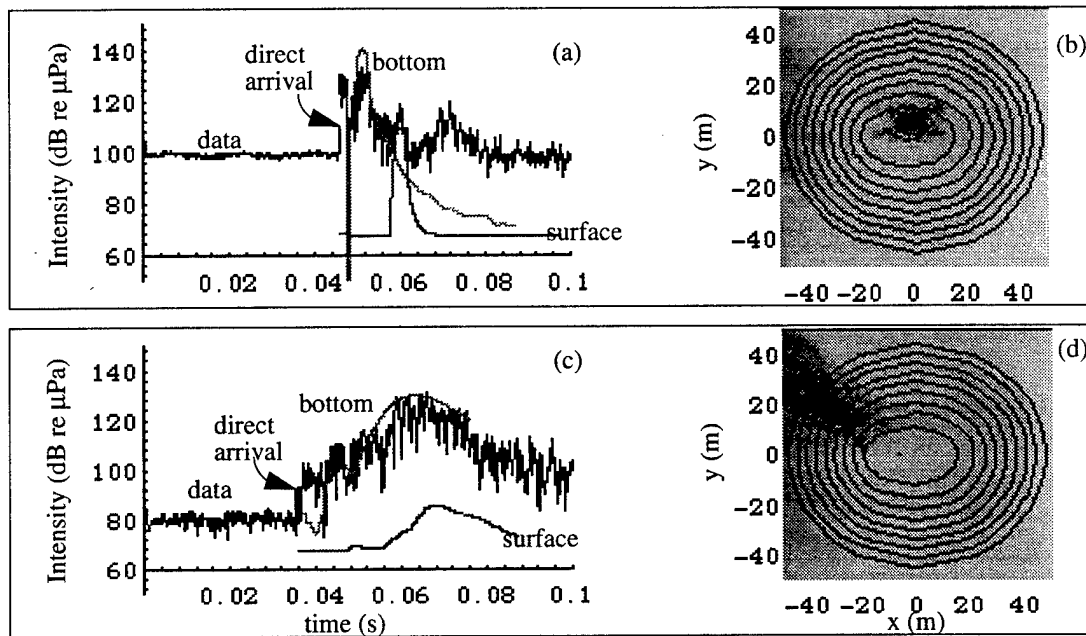
Figure 5. Model/data comparisons from the Panama City sand site and corresponding integrands of Eq. 23. Parts (a) and (c) show experimental waveforms along with simulations of the bottom- and surface-scattered signals based on Eq. 27 (see text for details). The vertical axis is the absolute level at the face of the receiver. Parts (b) and (d) show the integrand of Eq. 23 for the geometries of (a) and (c), respectively. The transmitter and receiver are along the y = 0 axis symmetrically placed around x = 0. The dark-gray regions indicate integrand values at least 30 dB higher than the light-gray regions. The ellipses indicate regions of the surface that contribute 4, 8, 12 ms, etc., after the initial bottom-scattered arrival.

The air/water signal was calculated with Eq. 27 using only the surface-roughness-scattering component of the bistatic model and roughness, sound speed, and density parameters typical of the ocean/air surface. This calculation was intended to give the signal's time of arrival relative to that of the bottom signal and to quantitatively assess its possible contamination of the bottom signal. Near forward scattering (Figure 5a), the air/water signal arrives well after the bottom signal; near backscattering (Figure 5c), the air/water signal is of much lower amplitude than the bottom signal. Thus contamination of the bottom signal is mitigated both by time separation and by beam-pattern effects. Similar checks of other geometries demonstrated that the data examined here were not significantly affected by air/water interface scattering.

Figures 5b and 5d are plots, in decibels, of the integrand in Eq. 23 for the curves shown in Figures 5a and 5c, respectively. Superimposed are ellipses showing the region of the seabed contributing to the signal received 4, 8, 12 ms, etc., after arrival of the initial bottom-scattered signal. This type of figure allowed a quick determination of whether the scattering was sufficiently localized that a definite set of bistatic angles (Figure 4) could be associated with the time of the peak bottom-scattered intensity. When this was possible, the bistatic angles were determined, and the difference between the theoretical prediction and the data was used to derive an experimental value for the bistatic scattering strength. This method has the advantage of being straightforward, but it is not applicable at some geometries. In particular, there are many cases where the scattering includes significant contributions from two regions: (1) from the main lobes of the two beams, and (2) from the sidelobes of the beams in combination with the peak in bistatic cross section in the forward direction. Near backscattering, the region making a significant contribution can be quite large; however, the times at which various regions contribute vary significantly, so time was used to help determine specific bistatic angles and associated scattering strengths. The bistatic angles for which data were obtained allow an assessment of the model's predictive capability for the experimental sites.

This method has an inherent advantage over sonar-equation-type analyses used to obtain scattering strength. In a sonar-equation calculation, one must make some estimate of the surface area that is contributing to the signal. Furthermore, if the bistatic scattering strength is varying over the ensonified area, it is a challenge to account for this effect. In carrying out the integral to predict the intensity time series, this is all implicitly taken into account.

Backscattering is a special case of bistatic scattering. Experimental backscattering values were obtained using the tower as both a transmitter and a receiver. In the following sections, both the backscattered data and the bistatic data are shown for each site. The Panama City site is examined first, since the sediment was more in keeping with the model assumptions. Tables of the experimental results are given in the appendix.

4.1. Panama City Site

In Figure 6, model predictions of bistatic scattering strength are plotted as a function of ϕ and θ_s for incident angles of 5°, 20°, and 60°. All experimental values for incident angles within ±2.5° of these angles are plotted as points for comparison with the model. Three views are shown for each incident angle so that data above and below the predictions can be seen. The data points are about 4 dB in diameter. The agreement between the data and the model predictions is sufficient to confirm much of the overall angular dependence predicted by the model. The 5° data show that the angular dependence and scattering level are well predicted for small incident and scattered grazing angles. The 20° data suggest that the increase in scattering predicted near forward scattering is also being captured. All three data sets suggest that the plateau predicted by the model for combinations of incident and scattered angles that are not near forward scattering and that are not too small is correct. However, the 20° data indicate that the plateau predicted by the model may be too high. All of these conclusions are retained when the full data set is examined.

An alternative method of examining the data is shown in Figure 7, in which all data for incident and scattered angles within specified ranges have been grouped and plotted as a function of ϕ. Model predictions were then calculated using $\theta_i = \theta_s$ for the lower and upper ends of each range. In Figure 7a, for example, the upper curve is for $\theta_i = \theta_s = 10°$ and the lower curve is for $\theta_i = \theta_s = 5°$. This technique eliminates data where the incident and scattering angles are not similar but does allow a simpler view of the data/model comparison. This view of the data again indicates an overall agreement between the model and the data, but Figure 7b still implies that the model's predictions for the plateau level may be slightly high.

4.2. Eckernförde Bay Site

The bubbles contained in the Eckernförde Bay mud have been identified as the major contributors to the backscattering,[28] and it is physically reasonable to assume the same is true for bistatic scattering. The model described in Section 1 was not developed to address strong scatterers within the sediment volume, so its applicability for this site is questionable. It is still valid to use Eq. 27 as a starting point in determining experimental values for the bistatic scattering strength. In this case, the model and the parameters given in Table 1 for this site can be viewed simply as a complicated means of obtaining an initial estimate.

Even though the model does not explicitly handle bubbles, it does allow volume scatterers that have both monopole and dipole components.[30] The model developed explicitly for this type of sediment structure by Chu and Tang and documented by Chu et al.[31] indicates that, for the frequency being used, the monopole and dipole components of the bubbles are the primary contributors to the scattering. This fact motivated the plots of experimental data and model predictions shown in Figure 8 made using the method used for Figure 7. The model curves use the parameters given in Table 1 for Eckernförde Bay.
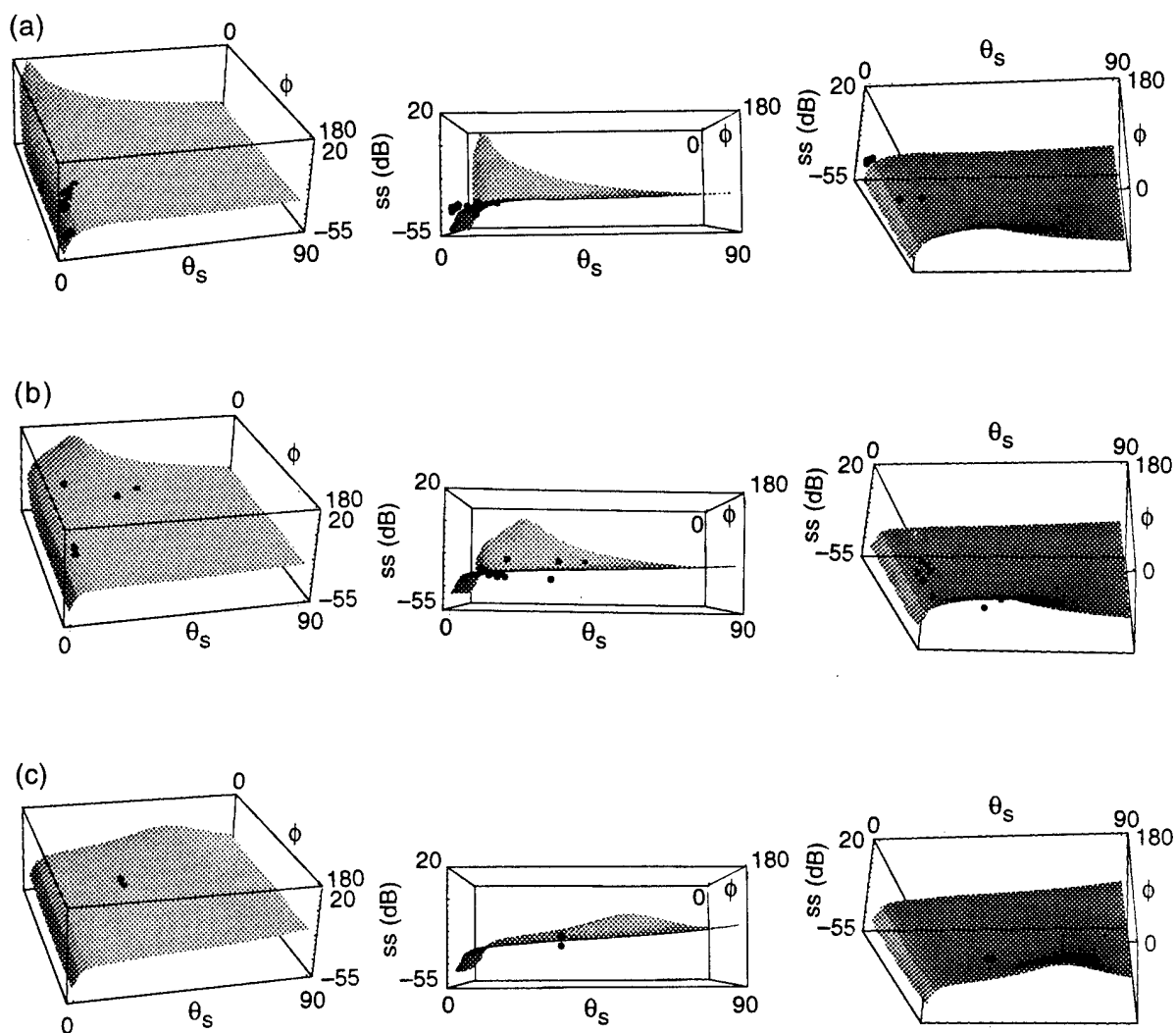
Figure 6. Model predictions of scattering strength (Eq. 1) for incident angles of (a) 5°, (b) 20°, and (c) 60°, shown as surfaces, and the experimental data from the Panama City site, shown as points. Three views are given for each plot so that the locations of all data point can be seen. See text for further discussion.

Though it is not useful to dwell long on the model/data comparison, examination of the figure demonstrates that, at the least, the model is not in obvious conflict with the overall behavior of the data.
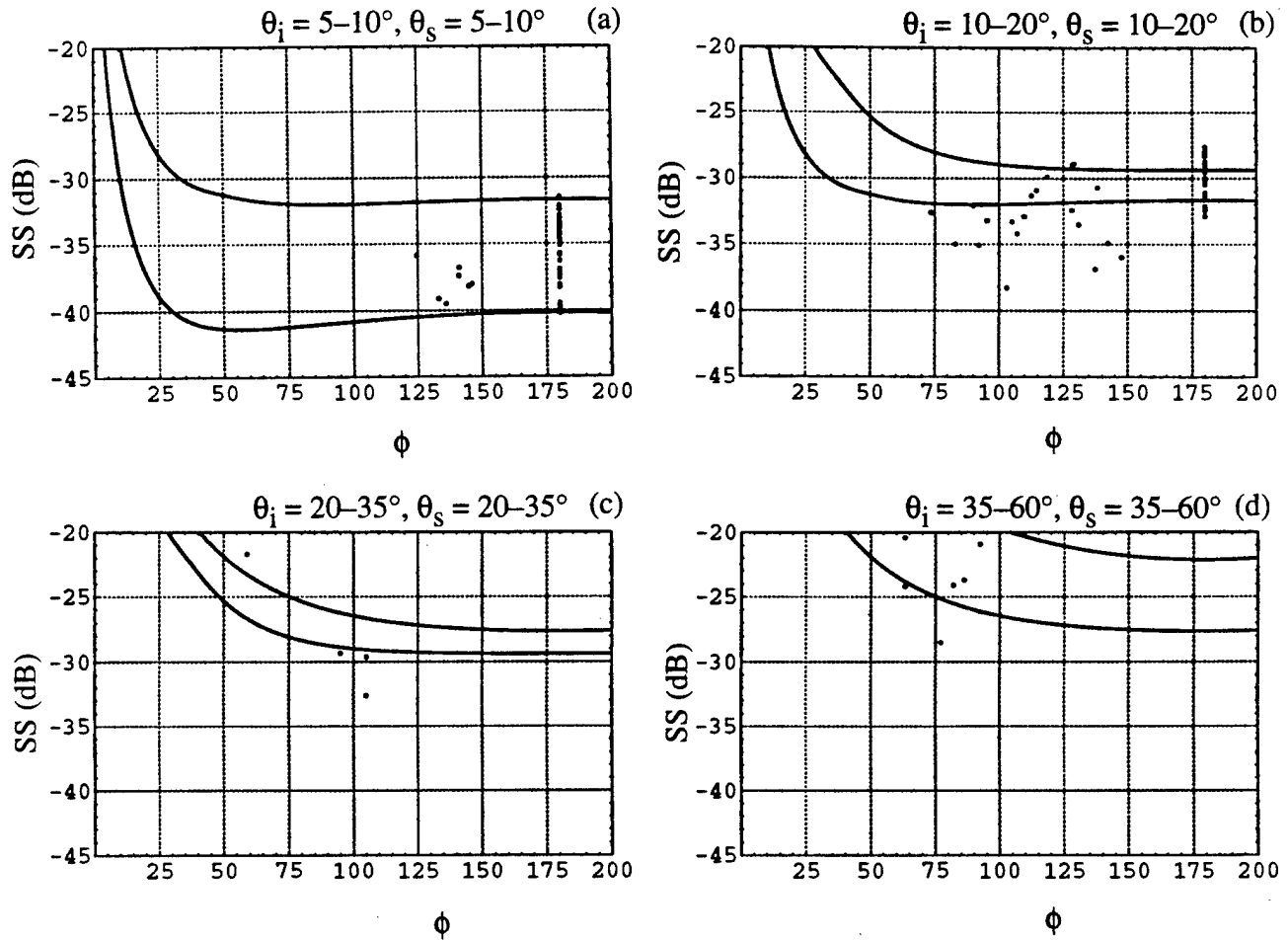
Figure 7. Model predictions of scattering strength compared with experimental data from Panama City site. Model predictions, shown as curves, are for the upper and lower values of the grazing angles given at the top of the figure (see Table 1 for site parameter values).
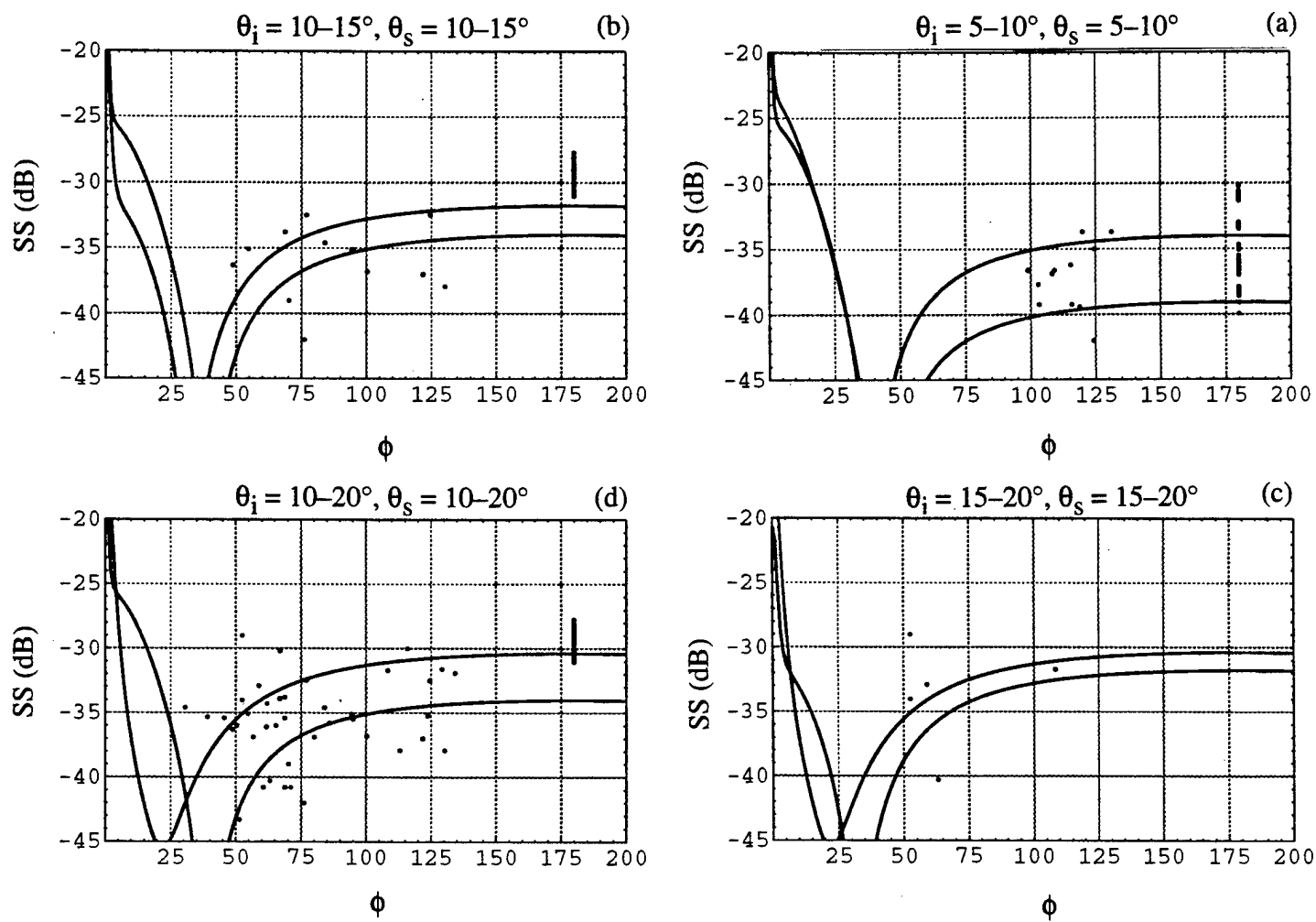
Figure 8. Same as Figure 7, but for Eckernförde Bay.

5. CONCLUSIONS

A model has been presented for describing bistatic scattering from ocean sediments. The model has its genesis in the backscattering model of Ref. 2. The model has been tested using data from two different sites visited as part of the Coastal Benthic Boundary Layer program. One of the sites had a bottom composed of coarse-grained sand; the other was a gassy mud. Of the two sites, the one with coarse sand better follows the assumptions of the model. For this site, the overall agreement between the model and the experimental data is good, with some indication that the model overpredicts the bistatic scattering by a few decibels at some angles (see Section 4.1). A comprehensive list of the bistatic experimental results is included in the appendix for both the sand and mud sites for use in testing alternative bistatic models.

In the case of the gassy-mud site, gas bubbles within the sediment contribute most of the scattering.[28] The agreement between the model and the data (shown in Figure 8) is sufficient for the model to be of practical use for this site, even though in this case it should not be viewed a fundamental physical model. The more physically correct model of Chu et al.[31] was compared with our experimental intensity time series to determine bistatic cross sections referenced back to the bubble layer (i.e., refraction and attenuation within the sediment are taken into account). One conclusion from this comparison is that inclusion of multiple scattering may be needed to fully model the Eckernförde site.

6. REFERENCES

1. D. R. Jackson, D. P. Winebrenner, and A. Ishimaru, "Application of the composite roughness model to high-frequency bottom backscattering," *J. Acoust. Soc. Am.*, **79**, 1410–1422, 1986.

2. P. D. Mourad and D. R. Jackson, "High frequency sonar equation models for bottom backscatter and forward loss," *Proc. OCEANS'89*, 1168–1175, 1989.

3. D. R. Jackson and K. B. Briggs, "High-frequency bottom backscattering: Roughness versus sediment volume scattering," *J. Acoust. Soc. Am.*, **92**, 962–977, 1992.

4. D. R. Jackson, "Models for scattering from the sea bed," *Proc. Inst. Acoust.*, **16**, 161–169, 1994.

5. A. N. Ivakin and Y. P. Lysanov, "Underwater sound scattering by volume inhomogeneities of a bottom medium bounded by a rough surface," *Sov. Phys. Acoust.*, **27**, 212–215, 1981.

6. P. C. Hines, "Theoretical model of acoustic backscatter from a smooth seabed," *J. Acoust. Soc. Am.*, **88**, 324–334, 1990.

7. D. Tang, "Acoustic Wave Scattering From a Random Ocean Bottom," Ph.D. thesis, Massachusetts Institute of Technology and Woods Hole Oceanographic Institution, June 1991.

8. A. P. Lyons, A. L. Anderson, and F. S. Dwan, "Acoustic scattering from the seafloor: Modeling and data comparison," *J. Acoust. Soc. Am.*, **95**, 2441–2451, 1994.

9. E. I. Thorsos, "Acoustic scattering from a 'Pierson-Moskowitz' sea surface," *J. Acoust. Soc. Am.*, **88**, 335–349, 1990.

10. A. Ishimaru, *Wave Propagation and Scattering in Random Media*, Vol. 2 (Academic Press, New York, 1978).

11. E. I. Thorsos, "The validity of the Kirchhoff approximation for rough surface scattering using a Gaussian roughness spectrum," *J. Acoust. Soc. Am.*, **83**, 78–92, 1988.

12. E. Y. T. Kuo, "Wave scattering and transmission at irregular surfaces," *J. Acoust. Soc. Am.*, **36**, 2135–2142, 1964.

13. A. N. Ivakin and Yu. P. Lysanov, "Theory of underwater sound scattering by random inhomogeneities of the bottom," *Sov. Phys. Acoust.*, **27**, 61–64, 1981.

14. J. E. Moe and D. R. Jackson, "First-order perturbation solution for rough surface scattering cross section including the effects of gradients," *J. Acoust. Soc. Am.*, **96**, 1748–1754, 1994.

15. J. H. Stockhausen, Scattering From the Volume of an Inhomogeneous Half-Space, Report No. 63/9, Naval Research Establishment, Canada, 1963.

16. A. Ishimaru, *Wave Propagation and Scattering in Random Media*, Vol. 1 (Academic Press, New York, 1978).

17. O. D. Grace and S. P Pitt., "Sampling and interpolation of bandlimited signals by quadrature methods," *J. Acoust. Soc. Am.*, **48**, 1311–1318, 1970.

18. D. R. Jackson and J. G. Dworski, "An acoustic backscatter thermometer for remotely mapping seafloor water temperature," *J. Geophys. Res.*, **97**, 761–767, 1992.

19. D. R. Jackson, K. L. Williams, and K. B. Briggs, "High-frequency acoustic observations of benthic spatial and temporal variability," *Geo-Marine Lett.*, **16**, 212–218, 1996.

20. R. Stein, "A modular acoustic measurement equipment system," *Proc. Oceans'83*, 176–181, 1983.

21. National Instruments Corporation, Austin, Texas.

22. Proceedings of the Gassy Mud Workshop, T. F. Wever (Ed.), Report 14, Federal Armed Forces Underwater Acoustics and Marine Geophysics Research Institute, Germany, 1994.

23. K.B. Briggs and M.D. Richardson, "In situ and laboratory measurements in Eckernfoerde Bay," in Proceedings of the Gassy Mud Workshop, T. F. Wever (Ed.), Report 14, Federal Armed Forces Underwater Acoustics and Marine Geophysics Research Institute, Germany, 1994, pp. 39–46.

24. H. M. Fielder and I. H. Stender, "The absorption layer in Eckernfoerde Bay sediments," in Proceedings of the Gassy Mud Workshop, T. F. Wever (Ed.), Report 14, Federal Armed Forces Underwater Acoustics and Marine Geophysics Research Institute, Germany, 1994, pp. 19–23.

25. J. A. Hawkins, D. N. Lambert, D. J. Walter, and J. C. Cranford, "Acoustic imaging of near-surface bubbly sediments," in Proceedings of the Gassy Mud Workshop, T. F. Wever (Ed.), Report 14, Federal Armed Forces Underwater Acoustics and Marine Geophysics Research Institute, Germany, 1994, pp. 54–58.

26. F. Abegg, A. Anderson, L. Buzi, A. P. Lyons, and T. H. Orsi, "Free methane concentration and bubble characteristics in Eckernfoerde Bay, Germany," in Proceedings of the Gassy Mud Workshop, T. F. Wever (Ed.), Report 14, Federal Armed Forces Underwater Acoustics and Marine Geophysics Research Institute, Germany, 1994, pp. 84–89.

27. A.L. Anderson, A.P. Lyons, L. Buzi, F. Abegg, and T. Orsi, "Modeling acoustic interaction with a gassy seafloor including examples from Eckernfoerde Bay, in Proceedings of the Gassy Mud Workshop, T. F. Wever (Ed.), Report 14, Federal Armed Forces Underwater Acoustics and Marine Geophysics Research Institute, Germany, 1994, pp. 90–94.

28. D. Tang, G. Jin, D. R. Jackson, and K. L. Williams, "Analyses of high-frequency bottom and subbottom backscattering for two distinct shallow water environments," *J. Acoust. Soc. Am.*, **96**, 2930–2936, 1994.

29. D. R. Jackson, K. B. Briggs, K. L. Williams, and M. D. Richardson, "Tests of models for high-frequency sea-floor backscatter," *IEEE J. Oceanic Eng.*, in press.

30. D. R. Jackson, A Model for Bistatic Bottom Scattering in the Frequency Range 10–100 kHz, APL-UW TR 9305, Applied Physics Laboratory, University of Washington, August 1993.

31. D. Chu, K. L. Williams, D. Tang, and D. R. Jackson, "High frequency bistatic scattering by subbottom gas bubbles," *J. Acoust. Soc. Am.*, in press.

APPENDIX
Tables Summarizing Backscattering and Bistatic-Scattering Results

Table A1. Summary of Eckernförde backscattering and bistatic scattering.

θ_i	θ_s	ϕ	σ	θ_i	θ_s	ϕ	σ	θ_i	θ_s	ϕ	σ	θ_i	θ_s	ϕ	σ	θ_i	θ_s	ϕ	σ	θ_i	θ_s	ϕ	σ	θ_i	θ_s	ϕ	σ
5	5	180.0	-38.21	6	6	180.0	-36.55	7	7	180.0	-35.01	8	8	180.0	-33.37	9	9	180.0	-31.32	10	10	180.0	-30.86	11	11	180.0	-30.39
12	12	180.0	-29.74	13	13	180.0	-28.82	14	14	180.0	-29.64	5	5	180.0	-38.12	6	6	180.0	-36.44	7	7	180.0	-34.83	8	8	180.0	-33.32
9	9	180.0	-31.22	10	10	180.0	-30.60	11	11	180.0	-30.28	12	12	180.0	-29.55	13	13	180.0	-29.01	14	14	180.0	-29.64	5	5	180.0	-38.43
6	6	180.0	-36.27	7	7	180.0	-34.83	8	8	180.0	-33.33	9	9	180.0	-31.27	10	10	180.0	-30.76	11	11	180.0	-30.33	12	12	180.0	-29.56
13	13	180.0	-28.79	14	14	180.0	-29.57	5	5	180.0	-37.87	6	6	180.0	-36.00	7	7	180.0	-34.82	8	8	180.0	-33.18	9	9	180.0	-31.11
10	10	180.0	-31.05	11	11	180.0	-30.21	12	12	180.0	-29.14	13	13	180.0	-28.62	14	14	180.0	-29.26	5	5	180.0	-38.33	6	6	180.0	-35.86
7	7	180.0	-34.70	8	8	180.0	-33.00	9	9	180.0	-31.08	10	10	180.0	-30.65	11	11	180.0	-30.21	12	12	180.0	-29.36	13	13	180.0	-28.95
14	14	180.0	-29.42	5	5	180.0	-39.09	6	6	180.0	-36.79	7	7	180.0	-35.07	8	8	180.0	-33.03	9	9	180.0	-31.04	10	10	180.0	-30.13
11	11	180.0	-29.46	12	12	180.0	-29.00	13	13	180.0	-28.56	14	14	180.0	-28.37	5	5	180.0	-39.93	6	6	180.0	-36.99	7	7	180.0	-35.52
8	8	180.0	-33.47	9	9	180.0	-31.02	10	10	180.0	-30.22	11	11	180.0	-29.52	12	12	180.0	-28.56	13	13	180.0	-27.72	14	14	180.0	-28.05
5	5	180.0	-38.59	6	6	180.0	-36.51	7	7	180.0	-34.92	8	8	180.0	-33.20	9	9	180.0	-30.83	10	10	180.0	-30.24	11	11	180.0	-29.73
12	12	180.0	-28.86	13	13	180.0	-28.12	14	14	180.0	-28.63	5	5	180.0	-38.43	6	6	180.0	-36.13	7	7	180.0	-34.83	8	8	180.0	-33.26
9	9	180.0	-31.17	10	10	180.0	-30.77	11	11	180.0	-30.29	12	12	180.0	-29.57	13	13	180.0	-28.68	14	14	180.0	-29.48	5	5	180.0	-38.52
6	6	180.0	-36.40	7	7	180.0	-34.95	8	8	180.0	-33.36	9	9	180.0	-31.22	10	10	180.0	-30.79	11	11	180.0	-30.33	12	12	180.0	-29.67
13	13	180.0	-28.81	14	14	180.0	-29.58	19.9	9.0	111.2	-32.4	19.3	9.2	106.9	-32.4	19.2	9.5	102.8	-34.4	17.6	9.6	101.3	-30.4	18.4	10.0	95.0	-35.5
15.7	11.6	80.1	-36.9	14.6	12.3	76.2	-42	14.5	12.9	70.2	-39	15.1	13.8	65.3	-36	17.9	13.2	50.4	-36	12.3	12.9	130.3	-37.9	13.2	14.3	124.5	-32.5
13.4	15.0	121.8	-37	14.4	16.2	116.0	-30	14.4	17.3	113.1	-37.9	15.1	18.4	108.4	-31.7	15.3	20.2	103.1	-29	16.1	20.3	100.4	-38.4	14.6	24.8	96.8	-33.4
15.8	24.4	92.0	-33.4	16.1	26.8	85.7	-32.2	15.9	28.5	83.0	-37.2	15.6	32.8	78.0	-29.1	17.7	28.7	72.7	-32.1	6.7	6.8	124.4	-42	7.0	7.5	119.1	-39.4
7.1	8.1	116.0	-39.2	7.7	8.8	109.2	-36.6	7.9	9.7	103.4	-39.2	9.9	9.2	99.0	-36.6	9.4	10.5	92.0	-37.6	8.6	11.6	91.1	-37.6	8.8	13.5	80.5	-34.3
8.5	15.1	77.9	-36.3	18.1	12.2	30.5	-34.6	10.1	5.6	171.1	-38.7	13.1	6.2	171.5	-37.3	14.3	6.5	167.8	-35.9	18.5	7.1	162.5	-37.9	11.2	5.9	167.6	-32.1
13.6	6.3	163.6	-36.1	13.9	6.5	160.4	-38.0	12.2	6.3	157.1	-37.6	13.8	6.7	151.8	-36.0	14.3	6.9	146.1	-35.8	16.4	7.2	141.9	-39.3	16.9	7.3	138.8	-41.1
19.5	7.7	132.5	-39.6	20.2	7.9	128.3	-37.6	20.2	7.9	128.3	-34.6	18.5	11.5	39.2	-35.3	15.0	12.2	48.8	-36.3	14.4	11.9	54.7	-35.1	17.1	10.6	60.6	-40.8
15.7	6.4	168.2	-35.1	15.5	6.5	165.6	-38.1	19.1	6.9	160.7	-37.7	14.4	6.8	149.7	-33.1	18.4	7.3	145	-33.2	18.3	7.5	140.1	-37.3	34.6	8.6	131.5	-30.2
37.1	8.8	123	-27.6	33.1	8.9	120.8	-28.8	34.5	9.2	112.3	-32.4	34.7	9.2	112.3	-34.1	35.3	10.4	85.2	-31.4	34.1	10.8	77.1	-32.2	34.3	10.9	77.1	-33.9
32.7	11.4	70	-32.1	22.1	12.3	72.1	-36.5	21.2	12.8	68.9	-36.7	20.3	13.3	66.1	-42.2	15.2	15.7	63.1	-40.3	13.5	17.9	56.7	-36.9	13.1	19.1	51.4	-43.3
12.2	21.5	46.7	-33.3	12.3	22	40.7	-35.5	10.7	31.5	48.4	-39	12.2	23.3	53.4	-38.9	12.4	21	58	-32.4	13.2	19	62.1	-34.3	13.4	17.7	66.8	-33.9
13.9	17	67	-30.2	14	15	77	-32.5	12.2	15	84.1	-34.6	15.4	12	86	-35.8	14.4	12	94.5	-35.1	13.1	11	100.4	-36.8	10.9	6.1	164.4	-39.6
11.9	6.4	159.8	-35.5	15.8	7.2	151.2	-37.9	12.8	20.7	40.0	-36.5	13.9	18.4	45.6	-35.4	15.8	15.9	52.5	-29.0	15.9	16.0	52.5	-34.0	16.4	15.2	58.9	-32.9
18.2	14.2	61.8	-36.1	18.4	13.5	68.8	-35.4	18.5	13.6	68.8	-40.8	19.5	13.3	71.1	-40.8	20.4	12.9	73.8	-41.5	22.3	12.2	80.3	-37.8	16.7	7.4	148.8	-36
18.3	7.7	143.3	-34.7	17.3	7.7	141.9	-34.9	18.6	7.9	135.4	-32.6	19.2	8.1	131.7	-33.5	18.4	8.2	127.5	-30.6	18.8	8.4	123.6	-30.5	19.1	8.6	119.6	-32.4
14.6	10.8	68.8	-33.8	16.7	9.7	76.8	-33.5	16.3	9.3	84.4	-29.5	14.2	9.0	91.6	-39.7	11.7	8.8	98.3	-36.2	9.7	8.8	103.1	-37.7	9.6	8.2	108.4	-36.9
9.5	7.5	115.4	-36.2	8.7	7.1	120.2	-33.7	8.4	6.7	124.7	-35.0	7.7	6.2	131.2	-33.7	15.9	47	96.1	-30.1	16.1	36.1	100.5	-33.3	16.3	29	105.6	-35.5
16.2	25	112	-38.7	14.5	28.5	117.3	-35.8	14.8	20.0	123.6	-35.2	13.6	19	129.3	-31.6	13.5	16	134.3	-31.9								

Table A2. Summary of Panama City backscattering and bistatic scattering.

θ_i	θ_s	ϕ	σ	θ_i	θ_s	ϕ	σ	θ_i	θ_s	ϕ	σ	θ_i	θ_s	ϕ	σ	θ_i	θ_s	ϕ	σ	θ_i	θ_s	ϕ	σ	θ_i	θ_s	ϕ	σ
5	5	180.0	-37.53	6	6	180.0	-37.04	7	7	180.0	-35.77	8	8	180.0	-34.80	9	9	180.0	-33.65	10	10	180.0	-32.11	11	11	180.0	-31.53
12	12	180.0	-30.47	13	13	180.0	-29.97	14	14	180.0	-27.95	15	15	180.0	-28.76	5	5	180.0	-39.46	6	6	180.0	-37.58	7	7	180.0	-36.2
8	8	180.0	-34.60	9	9	180.0	-33.33	10	10	180.0	-32.36	11	11	180.0	-31.29	12	12	180.0	-30.23	13	13	180.0	-29.52	14	14	180.0	-28.02
15	15	180.0	-28.06	5	5	180.0	-38.27	6	6	180.0	-37.30	7	7	180.0	-35.75	8	8	180.0	-34.38	9	9	180.0	-33.	10	10	180.0	-32.20
11	11	180.0	-31.21	12	12	180.0	-30.05	13	13	180.0	-27.88	14	14	180.0	-28.01	15	15	180.0	-28.07	5	5	180.0	-40.00	6	6	180.0	-37.28
7	7	180.0	-35.80	8	8	180.0	-34.24	9	9	180.0	-33.72	10	10	180.0	-32.39	11	11	180.0	-31.61	12	12	180.0	-29.59	13	13	180.0	-28.31
14	14	180.0	-27.90	15	15	180.0	-27.64	5	5	180.0	-40.21	6	6	180.0	-36.95	7	7	180.0	-35.85	8	8	180.0	-34.13	9	9	180.0	-33.12
10	10	180.0	-31.45	11	11	180.0	-31.43	12	12	180.0	-30.14	13	13	180.0	-29.07	14	14	180.0	-28.28	15	15	180.0	-28.01	5	5	180.0	-39.74
6	6	180.0	-38.09	7	7	180.0	-36.97	8	8	180.0	-35.11	9	9	180.0	-33.93	10	10	180.0	-32.87	11	11	180.0	-32.45	12	12	180.0	-31.11
13	13	180.0	-29.25	14	14	180.0	-29.06	15	15	180.0	-29.50	10.0	10.0	180.0	-32.11	15.0	15.0	180.0	-28.0	13.8	13.7	147.6	-36.0	15.2	14.6	142.3	-34.9
16.8	15.3	138.3	-30.7	18.9	16.3	130.9	-33.5	18.9	16.7	128.2	-32.4	21.5	17.6	121.7	-31.2	21.5	18.6	115.3	-34.1	25.0	19.6	108.8	-33.7	25.0	20.2	105.0	-32.6
25.0	20.2	105.0	-29.6	25.0	21.5	95.0	-29.3	17.7	33.4	45.7	-35.2	16.8	35.1	45.6	-32.2	16.8	37.2	39.7	-35.0	9.9	16.7	14.3	-36.3	11.7	18.6	137.5	-36.9
13.2	20.8	131.5	-37.6	16.0	22.2	125.7	-36.2	33.4	12.5	91.1	-35.0	17.8	12.7	93.1	-32.0	37.7	12.9	74.5	-30.2	37.7	13.2	63.7	-29.8	37.7	13.2	63.7	-29.8
20.1	14.3	65.2	-34.0	13.8	22.2	58.0	-31.4	13.2	23.0	57.3	-33.4	12.7	24.7	51.4	-32.7	12.2	25.6	45.6	-34.8	11.3	28.9	40.1	-29.9	5.5	8.7	146.0	-38.0
5.5	8.8	144.7	-38.2	5.9	9.4	141.0	-37.4	6.8	10.7	133.3	-34.4	7.5	12.0	125.3	-38.7	6.5	7.9	141.1	-36.8	6.5	8.3	136.0	-39.5	5.7	8.6	133.3	-39.1
6.6	9.8	124.6	-35.9	6.7	10.1	122.0	-42.7	7.5	10.9	115.9	-38.0	23.3	33.1	58.9	-21.7	22.1	36.3	51.8	-21.8	20.9	40.0	45.5	-27.7	18.8	45.9	40.7	-22.7
57.6	35.6	63.3	-20.4	58.2	36.2	63.3	-24.2	61.0	35.9	71.2	-22.7	57.5	36.0	77.1	-28.5	54.2	36.0	82.0	-24.1	51.1	36.0	86.2	-23.7	52.2	35.3	92.4	-20.9
49.6	34.5	101.2	-22.6	19.8	11.5	129.1	-28.9	18.3	11.5	128.3	-29.0	19.5	12.2	118.8	-29.9	18.2	12.5	114.5	-30.9	18.5	12.9	109.8	-32.9	15.9	12.7	112.6	-31.3
15.8	13.4	105.0	-33.3	14.8	13.3	107.1	-34.2	13.7	14.0	103.1	-38.3	13.0	15.2	95.4	-33.2	13.8	15.5	92.2	-35.1	13.5	16.0	89.9	-32.1	11.9	18.1	83.1	-35.0
11.2	20.5	76.4	-29.8	12.6	19.7	73.6	-32.6	20.5	16.8	26.0	-20.5	13.7	20.6	21.0	-20.7	6.1	11.4	126.3	-35.6	6.6	11.4	125.1	-35.0	6.5	12.6	121.0	-35.1
6.4	14.9	114.9	-34.8	6.8	16.6	108.7	-35.4																						

REPORT DOCUMENTATION PAGE

Public reporting burden for this collection of information is estimated to average 1 hour per response, including the time for reviewing instructions, searching existing data sources, gathering and maintaining the data needed, and reviewing the collection of information. Send comments regarding this burden estimate or any other aspect of this collection of information, including suggestions for reducing this burden, to Washington Headquarters Services, Directorate for Information Operations and Reports, 1215 Jefferson Davis Highway, Suite 1204, Arlington, VA 22202-4302, and to the Office of Information and Regulatory Affairs, Office of Management and Budget, Washington, DC 20503.

1. AGENCY USE ONLY (Leave blank)	2. REPORT DATE July 1997	3. REPORT TYPE AND DATES COVERED Technical

4. TITLE AND SUBTITLE

Bistatic Bottom Scattering: Model, Experiments, and Model/Data Comparison

5. FUNDING NUMBERS

Contract N00039-91-C-0072
N00014-96-1-G901

6. AUTHOR(S)

by K.L. Williams and D.R. Jackson

7. PERFORMING ORGANIZATION NAME(S) AND ADDRESS(ES)

Applied Physics Laboratory
University of Washington
1013 NE 40th Street
Seattle, WA 98105-6698

8. PERFORMING ORGANIZATION REPORT NUMBER

APL-UW TR 9602

9. SPONSORING / MONITORING AGENCY NAME(S) AND ADDRESS(ES)

Edward D. Chaika, Code 3210A
Office of Naval Research Detachment
1020 Balch Boulevard
Stennis Space Center, MS 39529-7050

10. SPONSORING / MONITORING AGENCY REPORT NUMBER

11. SUPPLEMENTARY NOTES

12a. DISTRIBUTION / AVAILABILITY STATEMENT
Distribution unlimited.

12b. DISTRIBUTION CODE

13. ABSTRACT (Maximum 200 words)

A model is presented for bistatic scattering from ocean sediments. It treats scattering due to both roughness of the seabed and volume inhomogeneities within the sediment. Accordingly, the scattered intensity is assumed to be a sum of two terms, one proportional to the roughness-scattering cross section and the other proportional to the volume-scattering cross section. The model is tested against data acquired as part of the Coastal Benthic Boundary Layer (CBBL) research program. As part of that program, an autonomous, circularly scanning sonar system was deployed in well-characterized regions. This sonar operated at 40 kHz, had a 5° horizontal beam, and acquired backscattering data over a 50-m radius. During part of the deployment, it operated in conjunction with a mobile receiving array so as to acquire bistatic data. The experimental apparatus and procedures are presented, and results are compared with model predictions.

14. SUBJECT TERMS
Bistatic scattering, roughness, ocean sediments, 40 kHz, volume inhomogeneities

15. NUMBER OF PAGES
31

16. PRICE CODE

17. SECURITY CLASSIFICATION OF REPORT Unclassified	18. SECURITY CLASSIFICATION OF THIS PAGE Unclassified	19. SECURITY CLASSIFICATION OF ABSTRACT Unclassified	20. LIMITATION OF ABSTRACT SAR